JAAS

PAPER

View Article Online
View Journal | View Issue

Cite this: J. Anal. At. Spectrom., 2025, 40, 1258

$^{40}Ar/^{39}Ar$ dating of volcanic fallout under seawater: influence of glass†

Zhiyu Han, *[ab] Fei Wang, [ab] Liekun Yang,[ab] Wenbei Shi[ac] and Yinzhi Wang[ac]

Accurate dating of submarine volcanic rocks is crucial for understanding many geological processes. However, some submarine volcanic rocks yield inaccurate young $^{40}Ar/^{39}Ar$ ages. To address this issue, we conducted $^{40}Ar/^{39}Ar$, electron microprobe and energy-dispersive X-ray spectroscopy analyses on hornblende, plagioclase and glass samples of the fallout tephra from borehole U1396A of the Integrated Ocean Drilling Program (IODP) 340 Expedition. Based on the $^{40}Ar/^{39}Ar$ analyses, 3 samples yield reasonable ages for the tephra, whereas the other 6 samples exhibit abnormally young ages. Remarkably, glass is widely present in hornblendes and plagioclases, as shown in the field emission scanning electron microscopy (FESEM) images. These glass samples have much higher K contents than the hornblende and plagioclase samples. Based on the K distribution of the glass, we propose that seawater can significantly increase the K content in some samples containing glass during the post-eruption period. Due to the extra addition of K, the determined $^{40}Ar/^{39}Ar$ ages of these submarine samples are predicted to be younger and are incorrect. In this study, an effective pretreatment method is proposed to reduce the effect of glass on the $^{40}Ar/^{39}Ar$ dating of the hornblende samples. The three hornblende samples subjected to our pretreatment method have all yielded more reliable $^{40}Ar/^{39}Ar$ ages, which suggests that our pretreatment method has the potential to enable more submarine volcanic rock samples to produce trustworthy $^{40}Ar/^{39}Ar$ age determinations in the future.

Received 6th February 2025
Accepted 5th March 2025

DOI: 10.1039/d5ja00045a

rsc.li/jaas

1. Introduction

Isotopic dating of submarine volcanic rocks has provided age constraints for many crucial geological processes in the evolution of the Earth; these processes include sea floor spreading, hot spot formation and the migration and evolution of subduction zones.[1–7] Especially as the Integrated Ocean Drilling Program (IODP) progresses, accurate dating of submarine volcanic rocks is needed.

The $^{40}Ar/^{39}Ar$ (K–Ar) method is one of the most commonly used isotopic dating methods due to the multiple types of volcanic products suitable for testing, for example, feldspars, mica, amphibole and volcanic glass.[8] This method has the potential to be a good solution for determining the ages of submarine volcanic rocks. However, in practice, when the $^{40}Ar/^{39}Ar$ (K–Ar) method is used to date submarine volcanic rocks, some samples produce inaccurate young apparent ages.[9–13] These erroneous apparent ages are often interpreted as resulting from either the addition of potassium (K) or the loss of argon (Ar) in submarine volcanic rocks due to submarine weathering, because in the K–Ar isotopic system, both the addition of the radioactive parent isotope (K) and the loss of the radiogenic daughter isotope (Ar) during subsequent geological processes can result in an underestimation of the apparent age of samples.[8] Unfortunately, in cases where samples have experienced K addition, it is difficult to verify whether Ar loss has occurred. Melson and Thompson (1973) observed that in a submarine environment, the alternation process leads to formation of secondary K-rich smectites within microfractures, which contribute additional potassium to the submarine basalts.[14] Consequently, these basalts show young apparent $^{40}Ar/^{39}Ar$ ages; these young ages result from the addition of parent isotopes. The formation of K-bearing altered minerals appears to be a reasonable cause for some unexpected young ages. Therefore, to avoid the influence of altered minerals on the $^{40}Ar/^{39}Ar$ analyses, researchers tend to use the least altered fraction for $^{40}Ar/^{39}Ar$ dating. However, even after careful selection, some analyzed samples continue to display apparent $^{40}Ar/^{39}Ar$ ages which are difficult to interpret.[7,15–18] These samples often show significant perturbations in the $^{40}Ar/^{39}Ar$ age spectra and possess inconsistent $^{40}Ar/^{39}Ar$ ages compared with stratigraphic limitations. In some cases, different minerals from the same volcanic rock display distinct ages. In summary, even after excluding the interference of alteration minerals, the $^{40}Ar/^{39}Ar$ dating results of submarine

[a]State Key Laboratory of Lithospheric and Environmental Coevolution, Institute of Geology and Geophysics, Chinese Academy of Sciences, Beijing, China
[b]College of Earth and Planetary Sciences, University of Chinese Academy of Sciences, Beijing, China
[c]Institutional Center for Shared Technologies and Facilities, Institute of Geology and Geophysics, Chinese Academy of Sciences, Beijing, China

† Electronic supplementary information (ESI) available: Table A1 shows the detailed results of $^{40}Ar/^{39}Ar$ analysis of 12 samples. Table A2 shows the major element content of hornblende, plagioclase and glass which were tested using an electron microprobe. Table A3 shows the major element contents of glass inside the minerals which were tested by energy-dispersive X-ray spectroscopy analyses. See DOI: https://doi.org/10.1039/d5ja00045a

volcanic rocks still exhibit anomalously young apparent ages. Researchers often attribute these erroneous apparent ages simply to the addition of potassium (K) or the loss of argon (Ar) during the post-eruption phase. While these explanations have their merits, they also raise several questions. For instance, how does the addition of potassium (K) occur in the samples, and to what extent does it affect the ages? Can samples really lose Ar without significant alteration? To address these questions, we conducted a detailed study of submarine volcanic rock samples from the Lesser Antilles Arc (LAA) region, including particle morphology of volcanic ash, along with $^{40}Ar/^{39}Ar$ dating, electron microprobe analysis (EPMA), electron microscope observation, and energy spectrum analysis (EDS) of hornblende, plagioclase, and volcanic glass samples. This article provides a new perspective on the inaccuracies in $^{40}Ar/^{39}Ar$ dating ages of submarine volcanic rocks. Furthermore, we developed an effective pretreatment method specifically for hornblende samples in submarine volcanic ash to enable these samples to yield more reliable $^{40}Ar/^{39}Ar$ ages.

2. Geological setting

The LAA formed from subduction of Atlantic oceanic crust beneath the Caribbean plate (Fig. 1) at a convergence rate of ~2 cm year^{-1}.[19,20] The arc is divided into two island chains to the north of Martinique. The eastern chain is an older extinct arc that is presently covered by limestone. The western chain is a younger active arc.[21] The westward jump of the volcanic front may have been related to the subduction of aseismic ridges.[22] To the south of Martinique, inactive and active volcanic centers are superimposed. A clear variation in rock types along the LAA can be observed. In the northern and central (Saba to St. Lucia) islands, the dominant rock type is andesite, with minor basalts, dacites and rhyolites. On the southern islands (St. Vincent to Grenada), basalts and basaltic andesites are predominant.[23]

The IODP Expedition 340 drilled boreholes at a series of sites along the LAA to examine the constructive and destructive processes of volcanic edifices in the LAA. Among them, borehole U1396 (16°30.49′N, 62°27.10′W) was drilled on a topographic high location of ~30 km southwest of Montserrat (Fig. 1). This location was ideal for reconstructing the long-term eruptive history of the northern LAA. The 1396A core stretches from the surface down to a depth of 134.9 m below the seafloor. The core consists of a sequence of hemipelagic sediments, tephra layers and volcanoclastic muds.[24,25] Pb isotope data show that the tephra layers in the borehole are mainly from volcanoes in Guadeloupe and Montserrat.[26]

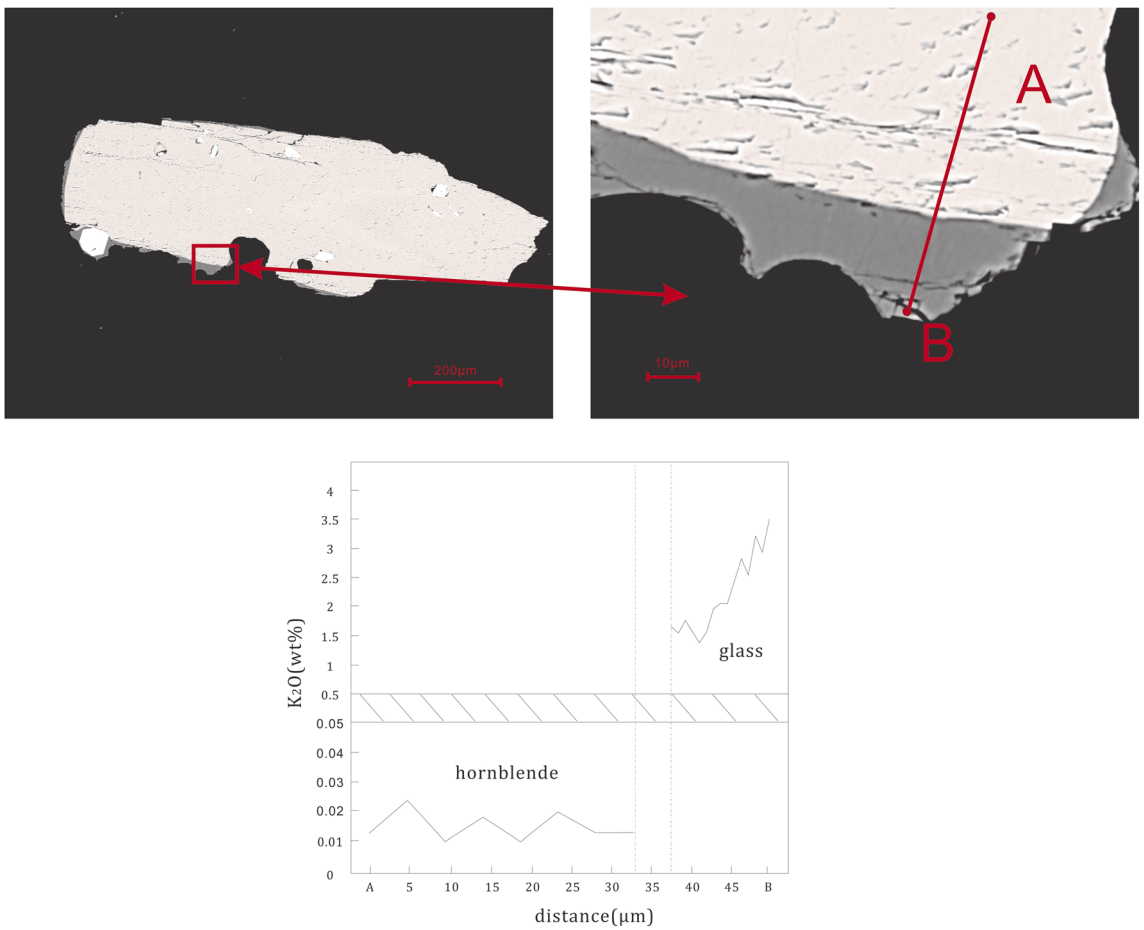

Fig. 1 Geological map of the Lesser Antilles arc. The red circle shows the geographic position of Site U1396. The dashed lines show the location of the older eastern arc and the recent western active arc.

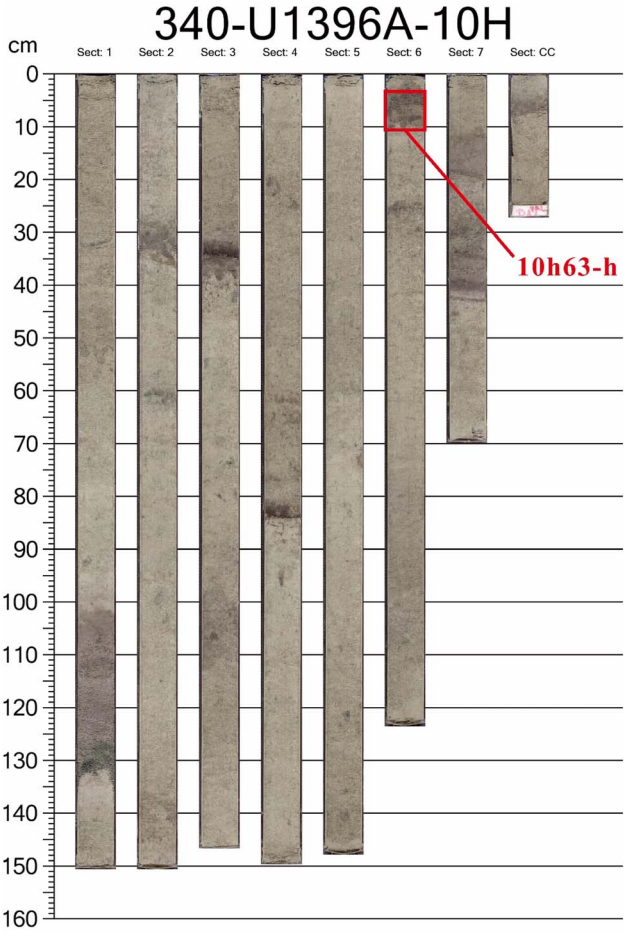

Fig. 2 Photo of core 1396A and the sample location of this sector.

Briden *et al.* (1979) reported a K–Ar age of 38–10 Ma in the outer arc (eastern chain), and the most inner arc (western chain) volcanic rocks had K–Ar ages of less than 3 Ma.[21] Zami *et al.* (2014) reported that a Les Saintes sample had a K–Ar age of 2.98 ± 0.04 Ma, and they claimed that this sample formed during the initial subaerial volcanic activity along the western chain of the LAA.[27] Harford *et al.* (2002) conducted $^{40}Ar/^{39}Ar$ tests on groundmass samples from Montserrat and identified three volcanic centers in Montserrat: Silver Hills, Central Hills and South Soufriere Hills, with $^{40}Ar/^{39}Ar$ ages ranging from ~2.6 Ma to the present.[28] Samper *et al.* (2007) conducted the K–Ar Cassignol–Gillot technique on samples from Guadeloupe and obtained a time scale between 2.79 ± 0.04 Ma and 0.435 ± 0.008 Ma.[29] In summary, most subaerial volcanic rocks in Guadeloupe and Montserrat are less than 3 Ma in age. However, paleomagnetic records from U1396A indicated that the volcanic activity began ~4.5 million years ago in the northern LAA;[30] therefore, this drill core provides a longer history of arc volcanism in the northern LAA dating back to the early Pliocene. Moreover, the Cenozoic volcanic ashes from core 1396A are ideal for investigating the effects of seawater on the $^{40}Ar/^{39}Ar$ ages because we can easily assess the accuracy of our dating results by comparing the deposition sequence of the layers and the corresponding paleomagnetic records.

3. Methods

The samples used for this study were obtained from borehole U1396A of IODP Expedition 340. The core image is shown in Fig. 2, and a detailed core description is provided by the Integrated Ocean Drilling Program Expedition 340 Preliminary Report.[24] The volcanic layers used for this study and the corresponding depths in the core are listed in Table 1.

3.1 Grain morphology

The volcanic layers in core 1396A include both primary volcaniclastic deposits and reworked volcaniclastic deposits. By examining the geometric features of the volcanic clasts, a quantitative method based on grain morphology was employed to identify the primary fallout tephra from the sedimentary sequence of the core in the LAA region.[31] The same analytical methodology as described by Cassidy *et al.* (2014) was adopted to analyze our samples. The sediment samples selected from the tephra layers in 1396A were first disaggregated, washed in deionized water, and then dried in an oven at 55 °C. Approximately 100 individual volcanic clasts from each layer were randomly selected and photographed under a stereo microscope with a digital camera in the $^{40}Ar/^{39}Ar$ and (U–Th)/He geochronology laboratory at the Institute of Geology and

Table 1 Sample name, correspondent depth in the core 1396A and grain morphology test results

Sample name	Depth CSF-A (m)	Number of analysis particles	Average perimeter (area)	Average aspect ratio (area)
4h773	34.33	79	19.50	27.64
6h558	50.18	139	57.53	194.34
7h620	60.80	136	75.87	393.31
10h1110	82.70	139	39.81	65.85
10h334	84.95	97	56.36	97.77
10h482	86.91	118	97.25	416.54
10h63	89.05	74	61.22	223.96
11h161	91.71	84	34.36	68.74
11h480	96.32	47	16.22	14.41
12h228	102.36	124	47.68	146.08
14h691	124.32	82	62.75	142.14

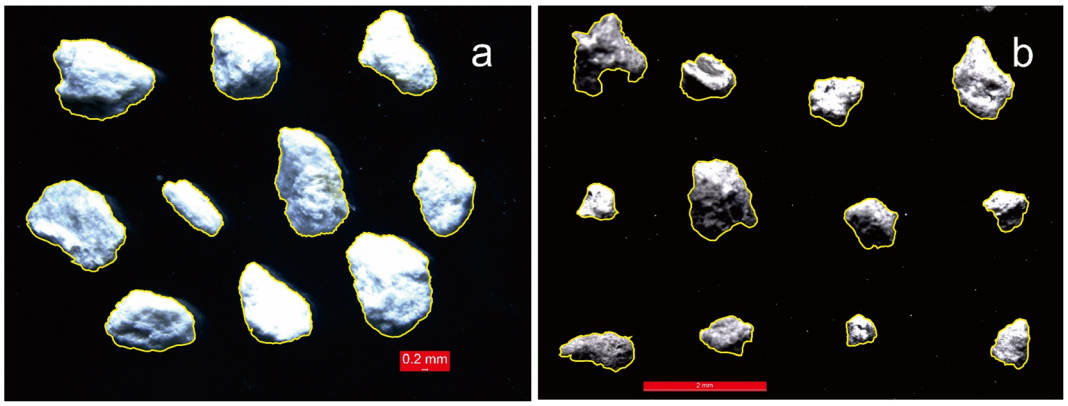

Fig. 3 Images processed using ImageJ software. The yellow lines show the calculated areas, which are enclosed using the 'magic wand' tool. (a) Image of the reworked sample of 4h773. (b) Image of the fallout sample of 10h1110.

Geophysics of the Chinese Academy of Sciences (IGGCAS). The images were processed with ImageJ software (Fig. 3). The area, perimeter and aspect ratio (longest axis/shortest axis) of these grains were recorded for image analysis.

3.2 $^{40}Ar/^{39}Ar$ analyses

One glass sample, 4 plagioclase samples and 4 hornblende samples from 9 different depths of volcanic layers were selected for the $^{40}Ar/^{39}Ar$ analyses. The information pertaining to the samples is listed in Table 2. Notably, glass widely exists in hornblendes and plagioclases, and these glasses significantly influence the $^{40}Ar/^{39}Ar$ dating results (see the discussion below). Hence, we designed two rounds of $^{40}Ar/^{39}Ar$ analyses for different purposes. In the first round, the aim was to determine the eruption age of tephra layers in 1396A, and the least altered fractions of the hornblende, plagioclase and glass samples from all 9 volcanic layers were carefully selected by handpicking using a binocular microscope. To mitigate the effects of nuclear recoil during irradiation, we predominantly use particles with a size greater than 200 μm. These separates were further washed in an ultrasonic bath in deionized water and then in acetone. Some of the samples were selected for subsequent irradiation, and the other parts were prepared for EPMA and EDS tests. In the second round, the aim was to reduce the influence of glass, and the hornblende samples of 10h1110h, 10h334h and 12h228h were mixed with high hardness carborundum, which had a smaller grain size than the hornblendes. These fractions were stirred using an electric blender at 1300 rpm for 12 hours to remove the glass (Fig. 4a). The fractions were subsequently subjected to sieving to eliminate the carborundum. This pretreatment process does not significantly affect the grain size

Table 2 Summary of $^{40}Ar/^{39}Ar$ analysis results[a]

Sample name	Material	Top depths CCSF-A (m)	Interpolated depositional age (Ma)	Total fusion age (Ma)	^{39}Ar (%)	Plateau age (Ma)	MSWD	Inverse isochron age	$^{40}Ar/^{36}Ar$ initials
First-round analysis results									
6h558g	Glass	56.06	2.44	2.12 ± 0.05	75.66	2.20 ± 0.06	1.27	—	281.5 ± 11.1
7h620-p	Plagioclase	67.82	2.73	2.61 ± 1.08	100.00	2.55 ± 1.07	1.30	2.22 ± 1.39	303.2 ± 28.5
10h1110h	Hornblende	92.07	3.38	1.78 ± 0.85	66.10	2.37 ± 0.75	0.71	—	292.6 ± 5.6
10h334h	Hornblende	94.56	3.44	2.48 ± 0.90	—	—	—	—	276.9 ± 12.3
10h482-p	Plagioclase	96.73	3.49	2.52 ± 1.75	85.42	1.36 ± 1.47	0.96	—	302.4 ± 21.4
10h63h	Hornblende	99.10	3.6	3.53 ± 1.22	84.43	3.41 ± 1.07	0.55	3.31 ± 2.30	298.4 ± 56.8
11h161-p	Plagioclase	102.04	3.6	2.77 ± 0.31	95.36	2.92 ± 0.29	0.57	—	277.7 ± 16.5
12h228h	Hornblende	113.83	3.8	3.15 ± 1.46	—	—	—	—	284.3 ± 25.8
14h691-p	Plagioclase	138.15	4.2	4.04 ± 0.65	97.44	4.04 ± 0.65	0.64	4.57 ± 1.34	277.7 ± 40.6
Second-round analysis results									
10h1110h-processed	Hornblende	92.07	3.38	3.27 ± 1.0653	53.81	2.79 ± 0.77	0.89	2.52 ± 0.90	308.7 ± 17.5
10h334h-processed	Hornblende	94.56	3.44	3.34 ± 1.12	85.73	3.21 ± 1.06	0.58	3.73 ± 2.33	294.6 ± 3.9
12h228h-processed	Hornblende	113.83	3.8	3.39 ± 0.74	—	—	—	3.47 ± 1.63	287.1 ± 110

[a] Errors are reported at the 2σ confidence level. The top depths CCSF-A and interpolated depositional age are calculated based on data of Hatfield (2015).

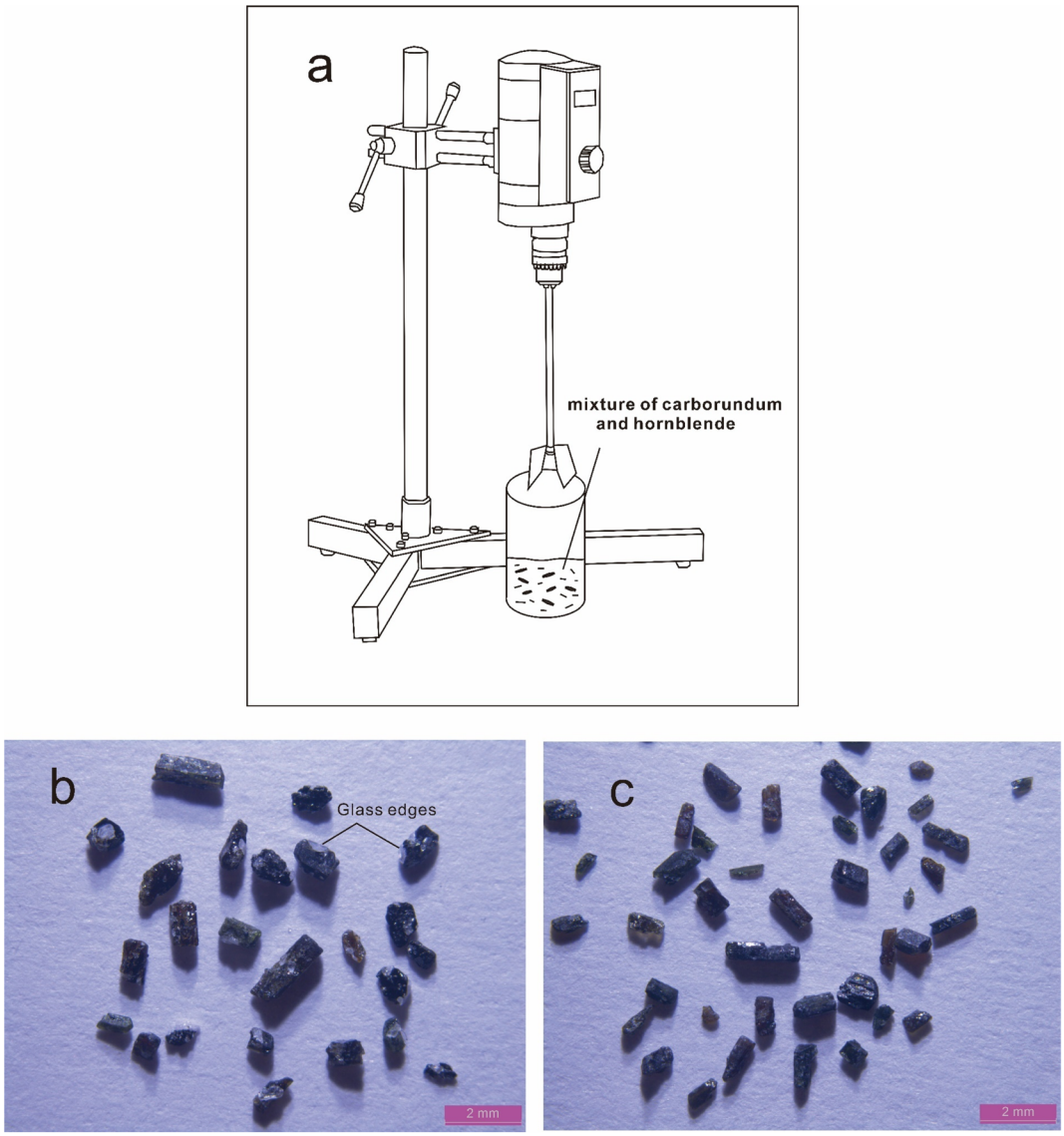

Fig. 4 Schematic diagram of the pretreatment equipment for the hornblende particles (a) and photographs of hornblende samples before (b) and after pretreatment (c). (b) Sample 10h1110h before pretreatment; (c) sample 10h1110h after pretreatment.

of the hornblende grains. Therefore, the processed hornblende samples exhibit grain sizes that are comparable to those of their untreated counterparts (Fig. 4b and c). Then we repeated the preparation steps above for the processed hornblende particles before the second irradiation.

All samples were wrapped in aluminum foil and then stacked in quartz vials with the international standard YBCs sanidine[32] (29.286 ± 0.045 Ma). The position of each sample was recorded as the distance from the bottom of the vial. The vials were subsequently sealed *in vacuo* and placed in an aluminum canister. The canister was wrapped with cadmium foil to shield the slow neutrons during irradiation.

For the first round, neutron irradiation was carried out at position B4 of the 49-2 Nuclear Reactor (49-2 NR), Beijing (China), for 4 h in December 2020. For the second round, neutron irradiation was carried out in a high-flux engineering test reactor (HFETR), Sichuan (China), for 5 h in July 2024. The J values for each sample are listed in Table A1, ESI.† Interference reactions during irradiation were checked by using pure CaF_2 and K_2SO_4; these samples produced the following correction factors: $[^{36}Ar/^{37}Ar]_{Ca} = 0.000269 \pm 0.0000015$, $[^{39}Ar/^{37}Ar]_{Ca} = 0.000709 \pm 0.0000020$, and $[^{40}Ar/^{39}Ar]_{K} = 0.00165 \pm 0.00011$ for the first-round irradiation and $[^{36}Ar/^{37}Ar]_{Ca} = 0.000230 \pm 0.0000078$, $[^{39}Ar/^{37}Ar]_{Ca} = 0.000660 \pm 0.0000010$ and $[^{40}Ar/^{39}Ar]_{K} = 0.00788 \pm 0.00025$ for the second-round irradiation.

The $^{40}Ar/^{39}Ar$ measurements were carried out at the IGGCAS, Beijing. After irradiation, the samples were removed from the vials and then placed on a high-purity copper disc. The disc was sealed in the chamber and maintained at ~140 °C for 4 days. The samples were heated using a CO_2 laser and degassed at 0.4 W for 30 s. We conducted 6 to 8 heating steps for each

sample to ensure the collection of a sufficient amount of gas at each step. The gas was purified with two Zr–Al pumps (SAES NP10). The purified gas was transferred to a Noblesse mass spectrometer for isotopic analysis. A decay constant of 5.543×10^{-10} year^{-1} for ^{40}K was used in the calculation of age.[33] The data were processed *via* ArArCALC software.[34] Errors are reported at the 2σ confidence level.

3.3 Electron microprobe and energy-dispersive X-ray spectroscopy analyses

For each sample, approximately 20 grains of hornblende, plagioclase, or glass were randomly selected and prepared as resin targets; the samples were set aside for further experiments.

The major element components of glass, hornblende and plagioclase were analyzed using a JXA8230 electron microprobe at IGGCAS, Beijing, China, with a voltage of 15 kV, a beam current of 20 nA, a spot size of 0 μm and a 10–30 s peak counting time. The natural minerals and synthetic oxides that were used for calibration were as follows: albite (Na and Al), bustamite (Mn), diopside (Ca, Si, and Mg), apatite (P), K-feldspar (K), rutile (Ti), and Fe_2O_3 (Fe). The spectral lines adopted for each element were as follows: Na (129.393 nm), Mn (146.186 nm), K (120.157 nm), Mg (107.399 nm), Si (77.371 nm), Fe (134.625 nm), Al (90.551 nm), Ca (107.907 nm), and Ti (88.751 nm). The detection limits (1 s) were 0.02 wt% for Mg, Al, Cr, K, Si, Mn, Ca and Fe and 0.04 wt% for the P. A program based on the ZAF procedure is used for data correction.

A high-resolution field emission scanning electron microscope (Zeiss Gemini 450) operating at 15 kV and a beam current of 2 nA was used to observe and image the microstructures of the samples. To eliminate charging and improve the contrast for low-density materials, a carbon coating of approximately 8 nm was applied to the samples using a coater system (Leica EM ACE600) to facilitate high-resolution FESEM imaging. To reveal the elemental distribution of the samples, energy-dispersive X-ray spectroscopy (EDS) data were collected with Oxford Ultim Max 60 mm^2 EDS detectors attached to the SEM at 15 kV. The EDS mapping was performed using an acceleration voltage of 20 kV, a beam current of 5 nA, a working distance of 8.5 mm, and a dwell time of 100 μs per point.

4. Results

4.1 Grain morphology

Due to the distinct transport processes of fallout and rework deposits, the volcanic clasts of these two types have distinct grain morphologies. Compared with those of reworked volcaniclastic deposits, the grains of tephra fallout deposits have greater angularity (perimeter length/area) and greater elongation (aspect ratio/area). The number of analyzed grains and the average angularity and elongation values are shown in Fig. 5 and Table 1. The reference line, which separates the reworked and fallout deposits, is from the study by Cassidy *et al.* (2014).[31] As shown in Fig. 5, most samples (9 of 11) fall within the range of primary tephra fallout deposits, with the exception of 11h480 and 4h773; these two samples fall within the range of reworked tephra. The fallout deposits can be distributed over a wide range and serve as stratigraphic markers.[35,36] A relationship between the deposition time and deposition depth of these fallouts in the core can be expected. Hence, the volcanic fallouts are ideal objects for ^{40}Ar/^{39}Ar dating. However, reworked volcaniclastic deposits can be emplaced on the sea floor without eruption,[37–41]

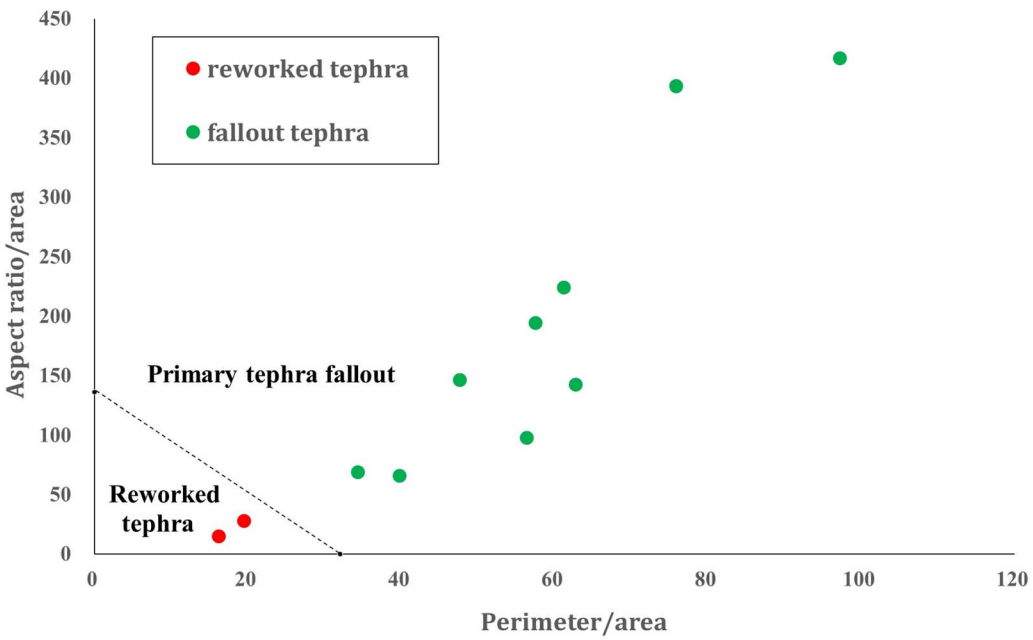

Fig. 5 Grain morphology test results. The dashed line shows the reference line that distinguishes primary tephra fallout and reworked tephra.[31] The two samples falling within the range of reworked tephra are 4h773 and 11h480.

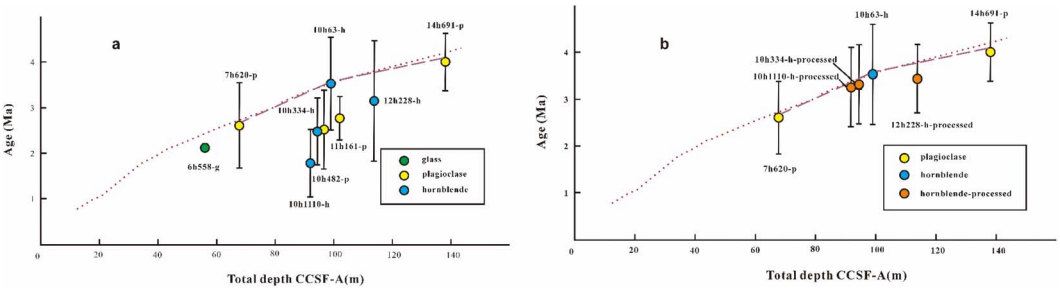

Fig. 6 Total fusion ages of the first round of $^{40}Ar/^{39}Ar$ analyses (a) and second round of $^{40}Ar/^{39}Ar$ analyses (b). In (b), the total fusion ages of the two plagioclases and 1 hornblende samples are also shown for comparison. The errors are reported at the 2σ confidence level. The red dashed line shows the age–depth relationship, which is defined by the paleomagnetic record.[30]

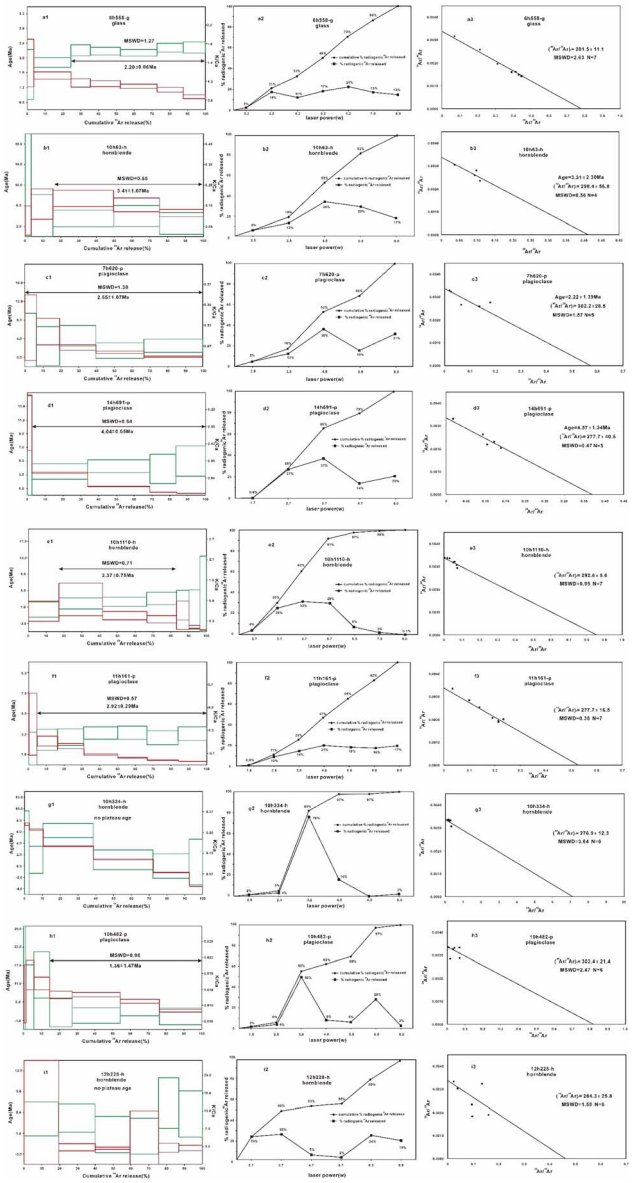

Fig. 7 Step-heating $^{40}Ar/^{39}Ar$ age spectra, K/Ca ratios, radiogenic ^{40}Ar release pattern and Ar isotope correlation diagrams of the glass, hornblende and plagioclase samples. Green lines are $^{40}Ar/^{39}Ar$ ages and red lines are K/Ca ratios.

dating tests on these layers yield meaningless ages. Thus, we selected the remaining 9 samples for the $^{40}Ar/^{39}Ar$ analyses and other tests.

4.2 $^{40}Ar/^{39}Ar$ analysis results

A detailed $^{40}Ar/^{39}Ar$ analysis of 9 unprocessed samples and 3 processed samples is provided in Table A1, ESI,† and a brief summary of the $^{40}Ar/^{39}Ar$ dating results is listed in Table 2. To assess the accuracy of the dating results, we also listed the paleomagnetic records of 1396A for comparison.[30] The interpolated depositional age was calculated by interpolating the adjacent ages of the polarity transitions. In this study, we define a plateau age as one that meets the following criteria in the step-heating Ar age spectrum: (1) the cumulative release of ^{39}Ar from three consecutive heating steps exceeds 50%; (2) the MSWD (Mean Square of Weighted Deviation) falls within the range of 0.5 to 1.5.[8,42]

The total fusion ages of the samples for the first-round $^{40}Ar/^{39}Ar$ analyses are shown in Table 2 and Fig. 6a. The total fusion ages of plagioclase samples 14h691-p (4.01 ± 0.65 Ma) and 7h620-p (2.61 ± 1.08 Ma) and hornblende samples 10h63h (3.53 ± 1.22 Ma) produce an age–depth relationship that is nearly the same as the paleomagnetic record. Moreover, within analytical uncertainties, these samples exhibit concordant plateau ages and inverse isochron ages that agree with the total fusion ages (Fig. 6 and 7b1–d3).14h691h has an age plateau of 4.04 ± 0.65 Ma and an inverse isochron age of 4.57 ± 1.34 Ma, 7h620-p has an age plateau of 2.55 ± 1.07 Ma and an inverse isochron age of 2.22 ± 1.39 Ma, and 10h63 has a plateau age of 3.41 ± 1.07 Ma and an inverse isochron age of 3.31 ± 2.30 Ma. The initial $^{40}Ar/^{36}Ar$ ratios ($(^{40}Ar/^{36}Ar)_0$) of 7h620-p (302.2 ± 28.5), 10h63h (298.4 ± 56.8) and 14h691-p (277.7 ± 40.6) are indistinguishable from the atmospheric value[43] (298.56) within the allowed error range. All evidence mentioned above indicates that the $^{40}Ar/^{39}Ar$ analyses of 14h691-p, 7h620-p and 10h63h provide reasonable age estimates of the corresponding eruptive activity.

In contrast, the glass samples (6h558g), 3 hornblende samples (10h1110h, 10h334h, and 12h228h) and 2 plagioclase samples (10h482-p and 11h161-p) produce clearly younger total fusion and plateau ages than the previously defined age–depth relationships (Fig. 6a, 7a1–a3 and e1–i3). Several laser heating steps of 10h334h, 10h482h and 12h228h result in a low

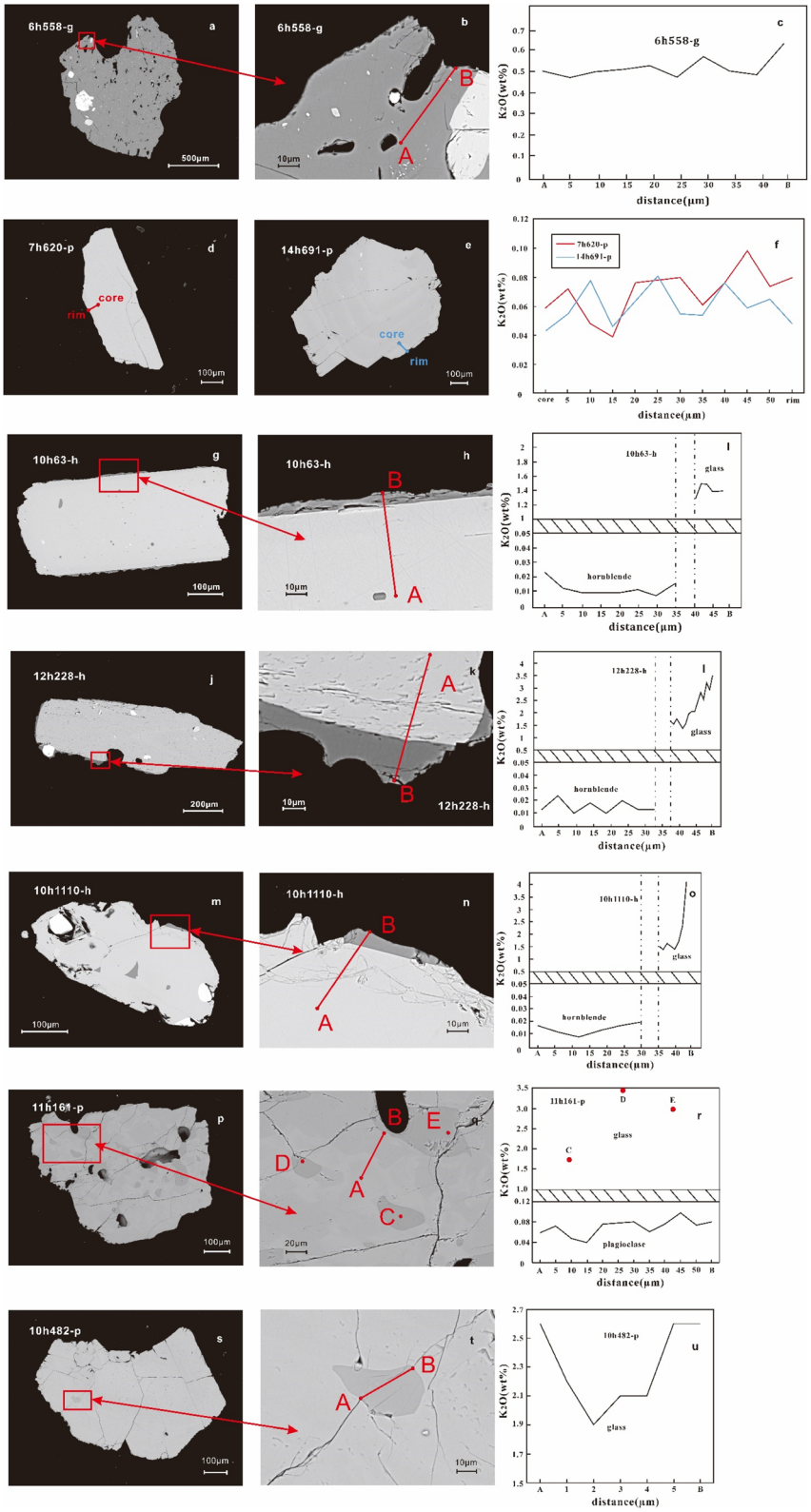

Fig. 8 Field emission scanning electron microscopy images and the K distribution in the glass, plagioclase and hornblende particles as following: glass sample 6h558-g (a–c), plagioclase sample 7h620-p (d–f), hornblende sample 10h63-h (g–i), hornblende sample 12h228-h (j–l), hornblende sample 10h1110-h (m–o), plagioclase sample 11h161-p (p–r), plagioclase sample 10h482-p (s–u).

proportion of radiogenic ^{40}Ar (<5%, Table A1, ESI†). Under these circumstances, a slight fluctuation of the argon blank during testing using the mass spectrometer can lead to intense changes in the age spectrum. This would make the interpretation of the age spectrum highly challenging. A more evident pattern of age change is observed from the age spectra of 6h558g, 10h1110h and 11h161-p. In the first 3–4 laser heating steps of these samples, the stage ages gradually increase from a young age to an older age. The initial $^{40}Ar/^{36}Ar$ ratios ($(^{40}Ar/^{36}Ar)_0$) of 10h1110h (292.6 ± 5.6), 10h482-p (302.4 ± 21.4) and 12h228h (284.3 ± 25.8) are indistinguishable from the atmospheric value, whereas the initial $^{40}Ar/^{36}Ar$ ratios of 6h558g (281.5 ± 11.1), 10h334g (276.9 ± 12.3) and 11h161-p (277.7 ± 16.5) are slightly lower than the atmospheric value. The inverse isochron ages of these younger-group samples are not given, and this aspect is further explained in the discussion section.

The second-round $^{40}Ar/^{39}Ar$ analysis results for the processed hornblende samples are shown in Fig. 6b and Table 2. Compared with the unprocessed samples, the processed hornblende samples present higher total fusion ages, from 1.78 ± 0.85 Ma to 3.27 ± 1.06 Ma for 10h1120h, 2.48 ± 0.90 Ma to 3.34 ± 1.12 Ma for 10h334h and 3.15 ± 1.46 Ma to 3.39 ± 0.74 Ma for 12h228h. The two processed samples, with defined plateau ages, also increase in age from 2.37 ± 0.75 Ma to 2.79 ± 0.77 Ma for 10h1110h and from no-plateau age to 3.21 ± 1.06 Ma for 10h334h. In addition, compared with their plateau ages, samples 10h1110h-processed and 10h334h-processed yield consistent inverse isochron ages within the allowed error range, and these values are 2.52 ± 0.90 Ma and 3.73 ± 2.33 Ma, respectively.

Notably, almost all samples in this study presented decreasing K/Ca ratios with increasing laser heating temperature (Table A1, ESI† and Fig. 7). This decreasing trend indicates that K and Ca are nonuniformly distributed in the samples.

4.3 K distribution in samples

The major element components of glass, plagioclase and hornblende tested using the electron microprobe are listed in Table A2, ESI,† and the 14 profiles of K_2O across specific ranges of the 8 samples are shown in Fig. 8.

In glass sample 6h558g, the K_2O content has an average value of 0.5137 wt% and shows a small variation range in the inner part of the grain (0.467–0.565 wt%), whereas in the outermost 5 μm portion, the K_2O content significantly increases and varies from 0.482 wt% to 0.627 wt% (Fig. 8a–c). For hornblendes, most samples have a K content of ~0.02 wt%; the K content fluctuates within a small range from the core to the rim, but no clear trend is observed (Fig. 8g–o). Plagioclases have a K_2O content of ~0.08 wt%, which is similar to that of hornblendes; additionally, a K content variation occurs inside the grains, but no clear trend is observed (Fig. 8d–f).

The FESEM images of the hornblende samples show no clear signs of alteration inside the mineral, but they reveal a noteworthy phenomenon. Most hornblende grains exhibit a glass edge surrounding the mineral particles (Fig. 8g, j and m). The thickness of these glass edges is usually a few microns to tens of microns. The EDS data revealed that the K_2O contents of these glass edges (~2 wt%) were several orders of magnitude greater than those of the hornblendes (~0.1 wt%) (note the difference between the EDS and electron microprobe data). We further tested the K distribution inside the glass edges of the hornblende sample. For each glass edge, we ran the analysis every 1 μm from the linkage between the glass edges and the hornblende to the rim. The results are shown in Table A3, ESI† and Fig. 8.

The K distributions of the glass edges are distinct in sample 10h63h and other hornblende samples. In sample 10h63h, the K_2O content has a narrow variation range from 1.3 to 1.5 wt% (Fig. 8g–i), while in samples 10h1110h, 10h334h and 12h228h, the K_2O content significantly increases from the innermost region to the rim of the glass edges (Fig. 8j–o). In sample 10h1110h, the K_2O content increases from 1.6 wt% to 4.0 wt%. In sample 10h334h, the K_2O content increases from 1.5 wt% to 2.1 wt%, and in sample 12h228h, the K_2O content increases from 1.8 wt% to 3.7 wt%.

Similar to the hornblendes, no alteration was observed inside the plagioclases. Glass also appears in some plagioclase samples but had different modes of occurrence. In samples 11h161-p and 10h482-p, glass exists mainly in the vitreous inclusions of the plagioclases (Fig. 8p and s). These inclusions normally have a diameter of a few microns to tens of microns, and many vitreous inclusions are in contact with the fractures in the plagioclases. In sample 7h620-p, no vitreous inclusions are observed, and in sample 14h691-p, the vitreous inclusions are small in size (Fig. 8d and e). The K_2O contents of the vitreous inclusions are closely

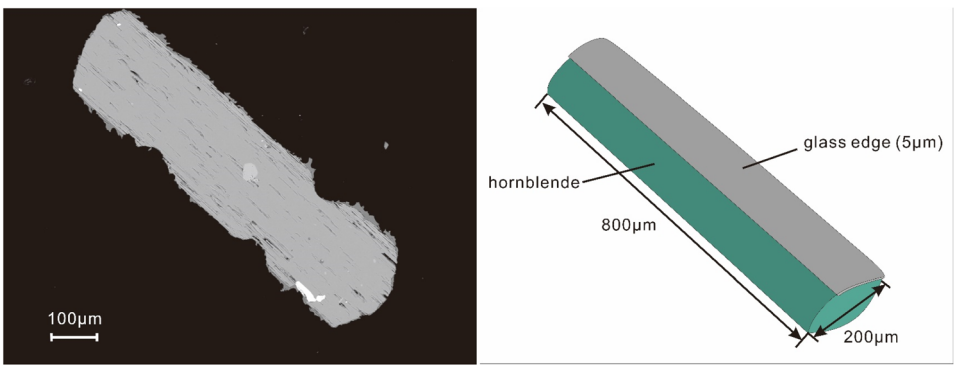

Fig. 9 Schematic diagram of the calculation method for estimating the K content of the glass edge of hornblende.

related to the fractures in plagioclase. The major element contents of 22 vitreous inclusions show that 10 of these inclusions are in direct contact with the fractures and the other 12 are isolated from fractures (Table A3, ESI†). Interestingly, these two groups of inclusions have distinct K contents. The K_2O content of the vitreous inclusions connected to the fractures is as high as ~3 wt%, whereas the K_2O content of the isolated inclusions is as low as ~1.5 wt% (Fig. 8p–r). For a case of a vitreous inclusion in sample 10h482-p that connects the fractures at its two ends, the K_2O content gradually increases from 1.9 wt% in the center to 2.6 wt% in both ends (Fig. 8s–u).

5. Discussion

5.1 Glass influence on the $^{40}Ar/^{39}Ar$ total fusion age

5.1.1 K change during the post eruption period. K is the parent isotope of $^{40}Ar/^{39}Ar$ isotopic dating. If the K content changes during the post-eruption period in a submarine environment, $^{40}Ar/^{39}Ar$ dating will yield an incorrect apparent age for the eruption timing. The volcanic glass inside hornblende and plagioclase usually results from the rapid cooling of magma,[44] and the $^{40}Ar/^{39}Ar$ ages of tested hornblende and plagioclase were actually mixed ages of hornblende or plagioclase and glass. If the glass maintains a closed system during the post-eruption period, it should share the same age with the hornblende or plagioclase and reflect the correct eruption time. Melson and Thompson (1973) reported that no compositional gradients were detected in the glass of Atlantic Sea Floor basalt, so they assumed that the glass was impermeable to major ions and molecules involved in the alteration of the glasses.[14] However, the strong variation in K observed in this study indicates that the glass could be an "open system" to K in seawater. Staudigel and Hart (1983) reported a high increase of K in basaltic glass during alteration undersea,[45] which is consistent with our observation. Here, a key problem is to determine the effect of this potential added K from the seawater to the glass on the $^{40}Ar/^{39}Ar$ dating results in the fallout volcanic clasts in seawater. The proportion of glass is relatively low compared with that of their host minerals; however, due to the difference in the orders of magnitude of the K content between the glass and their host minerals, glass could significantly contribute to the total Ar released in the dating experiments.

A simple evaluation of the influence of glass on the $^{40}Ar/^{39}Ar$ age can be performed. We assume that the hornblende is a regular cylinder and that the glass edges are cylindrical shells (Fig. 9). Assuming a hornblende grain in the shape of a cylinder with a diameter of 200 μm and a height of 800 μm, where only one-quarter of the hornblende is enclosed by a cylindrical glass shell with a thickness of 5 μm, and considering the typical K contents of glass (0.5 wt%) and hornblende (0.02 wt%), it can be calculated that the K content at the glass edge constitutes 40% of the total K content. Despite this inaccurate assumption, the role that glass plays in $^{40}Ar/^{39}Ar$ dating cannot be disregarded.

As mentioned above, the K content has extensively changed in the glass edges of the hornblende samples of 10h1110h, 10h334h and 12h228h. This variation can be attributed to an increase from the innermost region to the rim or a decrease from the rim to the innermost region. The latter variation means that K has diffused from glass to minerals; Ozima *et al.* (1977) reported a diffusion model to explain the co-reduction of K content and K–Ar age of submarine basalts from the surface to the interior.[12] He assumed that K had diffused from seawater into the basalt. If this process were to occur at the boundary between glass and hornblende as well, given that the potassium (K) content in the glass is much higher than that in hornblende, we would expect to observe a significant increase in potassium (K) content at the edges of the hornblende. However, we did not observe such a phenomenon (Fig. 8g–i). Hence, a more likely explanation is that K gradually increases from the inner region to the rim of the glass edge. The elevated K in the rim of glass sample 6h558g also supports this deduction (Fig. 8a–c). The extra addition of K after eruption significantly decreases the total $^{40}Ar/^{39}Ar$ fusion age. In contrast, no extra K is added to the glass edge in sample 10h63h, and the consistent total fusion age with the interpolated depositional age indicates that the glass and hornblende share similar ages. Thus, the $^{40}Ar/^{39}Ar$ age of 10h63h can represent the eruption time.

The K distribution in plagioclase samples can better clarify the possible source of this K variation. In samples 11h161-p and 10h482-p, the K contents of the vitreous inclusions tend to be higher when they are connected to the fractures of plagioclases (Fig. 8p–u). This relationship demonstrates that the fractures of plagioclase can provide pathways for seawater ion exchange with the vitreous inclusions, resulting in an increased K content in these samples and leading to a younger total fusion $^{40}Ar/^{39}Ar$ age. Dymond and Windom (1968) found plagioclase dates 25–50% younger than coexisting biotite in a dredged Pacific basalt sample; they attributed this difference to argon loss of plagioclase, although they could not rule out the possibility of potassium addition.[9] Regan *et al.* (2019) reported that some plagioclases showed slightly younger $^{40}Ar/^{39}Ar$ age (~47 Ma) compared to the coexisting pyroxene (~51 Ma); they interpreted 47 Ma to be a reheating age.[7] However, according to the observation of this study, the vitreous inclusions embedded in plagioclase are very difficult to eliminate (see more discussion in 5.3); the young apparent $^{40}Ar/^{39}Ar$ age may be caused by the vitreous inclusions with varying K content. In samples 7h620-p and 14h691-p, the vitreous inclusions are uncommon; thus, glass only has a slight effect on the $^{40}Ar/^{39}Ar$ age.

5.1.2 The possibility of argon loss during submarine alteration. The loss of Ar has always been considered to be one of the main factors leading to the young dating results of $^{40}Ar/^{39}Ar$ dating.[7,9,10,18,46,47] The age spectrum and Ar isotope isochron are usually used to judge whether Ar loss has occurred in the sample, but the addition of K in the sample will directly lead to the complexity of the interpretation of the age spectrum and isochron method.[8,48] However, through our pre-treatment experiment and geochronological data, we are able to address the question of whether Ar is lost in the dating target minerals during seafloor alteration.

In Fig. 6b, we showed the total fusion age of processed and unprocessed samples. The unprocessed samples, 10h63h, 7h620p and 14h691p, exhibit only a minor effect from altered glass, and we assumed that the influence of glass on the $^{40}Ar/^{39}Ar$ age of

processed samples (10h1110h, 10h334h and 12h228h) can be negligible. If significant Ar loss occurs in hornblende and plagioclase during seawater alteration, then they should give $^{40}Ar/^{39}Ar$ ages which are significantly younger than the stratigraphic reference age. However, our results showed that 5/6 samples gave $^{40}Ar/^{39}Ar$ total fusion ages which were highly consistent with the age–depth relationships which are defined by the paleomagnetic record. At least according to our results, Ar loss is not the main factor that causes the young apparent $^{40}Ar/^{39}Ar$ age.

5.2 Glass influence on the age spectra and isochrons

As we discussed above, the $^{40}Ar/^{39}Ar$ experiment on the so-called hornblende and plagioclase samples reflected the presence of a mixture of glass and its host minerals. The age spectra and K/Ca ratio of mixed phase samples can reveal different proportional contributions of different minerals, and a radiogenic ^{40}Ar release pattern diagram can help discuss the variations of ages, mineral phases and retentive sites.[49–53]

Most samples in this study showed a decrease in the K/Ca ratio as the laser heating temperature increased (Fig. 7). In calcium-rich minerals, the redistribution of ^{37}Ar and ^{39}Ar during irradiation can lead to a gradual decrease in K/Ca ratios with increasing step-heating temperatures.[54] However, according to Jourdan and Renne's (2014) study, such redistribution effects are more pronounced in fine-grained minerals (<5 μm).[54] In contrast, the majority of our mineral grains exceed 200 μm in size. Additionally, if the observed gradual decrease in K/Ca were caused by isotopic redistribution of ^{37}Ar and ^{39}Ar, it would typically coincide with progressively younger ages in the step-heating age spectra.[54] Such a trend, however, is not evident in our samples. In summary, we propose that the nuclear recoil of ^{37}Ar and ^{39}Ar during irradiation likely has negligible effects on K/Ca ratios and age determinations. Given that glass exhibits a higher K/Ca ratio (~0.2) than hornblende (~0.02) and plagioclase (~0.01), the observed decreases in K/Ca are more likely to reflect a diminished contribution of glass with increased heating temperature.

In the preceding discussion, we noted that the glass rim of sample 6h558g exhibits elevated potassium (K) content and yields younger total fusion and plateau ages. We propose that this sample effectively illustrates the contribution of glass within hornblende or plagioclase. Fig. 7a1–a3 display the age spectrum, K/Ca ratios, and radiogenic ^{40}Ar release pattern of glass 6h558g. Notably, the radiogenic ^{40}Ar release pattern remains relatively stable with increasing step-heating temperatures, indicating that the glass continues to degas even at high-temperature steps. Another distinct feature is the gradual decline in K/Ca ratios as step-heating temperature increases. The glass rim, which experienced K addition, initially shows higher K/Ca values. The observed decrease in K/Ca likely reflects a diminishing contribution of the K-enriched rim to the gas release. Furthermore, the K-enriched rim, compared to the glass interior, would yield lower $^{40}Ar/^{39}Ar$ ages. The hypothesis of reduced glass rim contribution at higher temperatures aligns with the progressively older step-heating ages observed. This inverse correlation between K/Ca and step heating age is particularly pronounced in the low-temperature steps, suggesting that K-enriched sites within the glass are preferentially degassed during early heating stages. However, we caution against dismissing glass rim effects at high-temperature steps, as the plateau ages at these stages remain younger than the reference age (Table 2).

The preferential release of Ar from altered glass during low-temperature steps is similarly evident in plagioclase and hornblende samples. Due to the low radiogenic ^{40}Ar content ($^{40}Ar_r$ < 5%) and low resolution (these samples tend to release most of the $^{40}Ar_r$ in 1 or 2 discontinuous steps) of the age spectra of 10h334h, 10h482-p and 12h228h, the correlations between K/Ca and the age spectra of these samples were not clear (Fig. 7g1–i3). A more distinct correlation in samples 10h1110h and 11h161-p was observed. In the first 5 stages for 11h161-p, the stage age gradually increased from 0.5 Ma to 3.14 Ma, and the K/Ca ratio decreased from 0.355 to 0.060. For hornblende sample 10h1110h, the first four-stage age increased from 0.41 Ma to 3.11 Ma, and the K/Ca ratio decreased from 0.596 to 0.355 (Fig. 7e1–f3). The covariation trend between step-heating ages and K/Ca ratios closely mirrors that observed in glass sample 6h558g during low-temperature steps, suggesting that the contribution of altered glass to argon release progressively diminishes with increasing temperature. This finding is further supported by our observation of a progressive increase in radiogenic ^{40}Ar release during low-temperature steps in both samples. Because, compared to glass, hornblende and plagioclase have a higher total content of radiogenic ^{40}Ar based on the assumption we made in Section 5.1.1. However, in sample 10h63h, the decrease in the K/Ca ratio was not accompanied by any increase in the step heating age (Fig. 7b1). This discrepancy was potentially caused by the distinct K distribution in the glass. For sample 10h63h, the glass edges showed no sign of K addition; glass and hornblende should have an identical age. Thus, the contribution proportion of glass change did not cause a fluctuation in the age spectrum. The sample 7h620-p exhibits similar change patterns to 10h63h. Compared to 11h161-p, sample 14h691-p exhibits a less pronounced trend of age variation with K/Ca ratios. Although these two samples still show decreased K/Ca ratios with increased step-heating temperature, the magnitude of decrease is significantly lower than that observed in other plagioclase samples (Fig. 7c1–d3), because 7h620-p and 14h691-p exhibit a limited effect of glass as demonstrated in Section 5.1.1.

We have shown the nonuniform distribution of K in the glass in some samples; due to the continuous ion exchange between the seawater and glass, the K atoms inside the sample have different decay times, resulting in a nonuniform distribution of ^{40}Ar in the samples. The Ar isotope correlation analyses of the inverse isochrons in these samples yield meaningless inverse isochron ages due to the poor linearity between the $^{36}Ar/^{40}Ar$ and $^{39}Ar/^{40}Ar$ ratios. However, the influence of glass in the Ar isotope correlation diagrams of 6h558g, 11h161-p and 10h334h can still be observed (Fig. 7a3, f3 and g3). These samples exhibit initial $^{40}Ar/^{36}Ar$ ratios ($(^{40}Ar/^{36}Ar)_0$), which are lower than the atmospheric values. If the samples remained in a "closed system" after eruption, they should have initial $^{40}Ar/^{36}Ar$ ratios ($(^{40}Ar/^{36}Ar)_0$), which are similar to the atmospheric values; however, the increased K values in these

samples lead to higher $^{39}Ar/^{40}Ar$ values at early laser heating stages, cause the isochron to shift upward, and finally produce a higher initial $^{36}Ar/^{40}Ar$ ratio of these samples.

5.3 Solutions to the effect of glass on the hornblende and plagioclase samples

We investigated the effects of glass on dating hornblende and plagioclase. Thus, minimizing the influence of glass is key to accurately dating submarine samples.

The glass occurs mostly as edges encircling the hornblende. Here, we designed a pretreatment method to remove the glass edges of hornblende. The detailed method is described in the Methods section above. Fig. 4b and c display photographs of the samples before and after pretreatment. The images demonstrate a noticeable reduction in glass content following the pretreatment process. The total fusion ages and age spectra of the 3 unprocessed hornblendes and 3 processed hornblendes are shown in Fig. 6. All three samples showed varying degrees of increase in total fusion age. The samples 10h1110h-processed and 10h334h-processed yielded total fusion ages of 3.27 ± 1.06 Ma and 3.34 ± 1.12 Ma, respectively; these ages were highly consistent with the age–depth relationships defined using 7h620-p, 10h63h and 14h691-p. Sample 12h228h-processed still provided a slightly younger total fusion age (3.39 ± 0.74 Ma); however, this age estimation was improved with respect to the unprocessed sample. Although we could not define a reliable plateau age for sample 12h228h-processed, samples 10h1110h-processed and 10h334h-processed yielded plateau ages of 2.79 ± 0.77 Ma and 3.21 ± 1.06 Ma, respectively; these ages were consistent with their total fusion ages and inverse isochron ages (2.52 ± 0.90 Ma for 10h1110h-processed and 3.73 ± 2.33 Ma for 10h334h-processed) within the allowed error range (Fig. 10a–d). These results indicated that our pretreatment method could effectively remove the glass edges of hornblende and yield high-quality $^{40}Ar/^{39}Ar$ data.

For plagioclase samples, the influence of glass was difficult to avoid because glass mostly was present inside plagioclase, and the majority of vitreous inclusions had a diameter of a few microns. To remove the vitreous inclusions, the plagioclase needed to be crushed into fine grains that could be removed. However, this process would cause serious ^{39}Ar loss from the

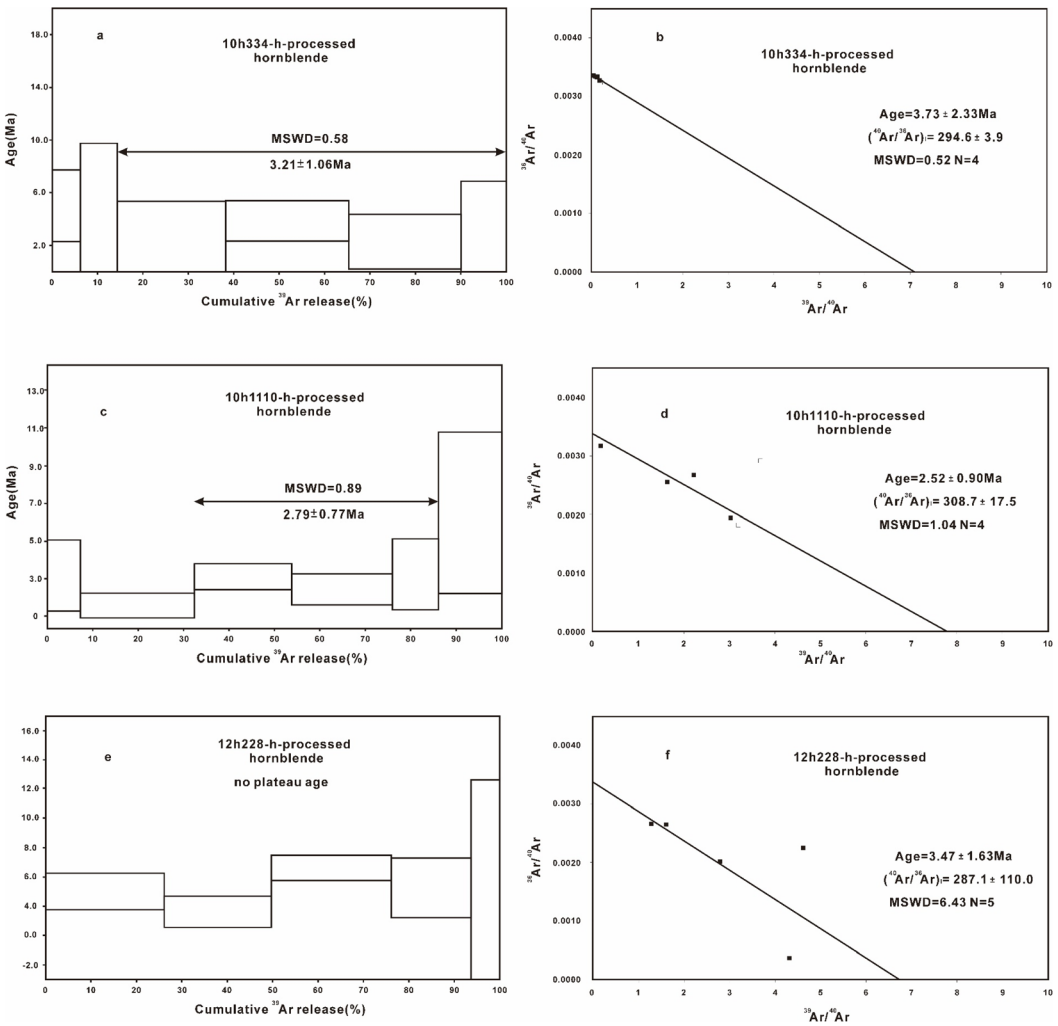

Fig. 10 Age spectra and inverse isochron diagrams of the following samples: 10h334-h-processed (a and b), 10h1110-h-processed (c and d) and 12h228-h-processed (e and f).

nuclear recoil effect during irradiation in a reactor before $^{40}Ar/^{39}Ar$ dating.[8,55,56] Therefore, for submarine plagioclase samples, detailed observations are needed to determine whether plagioclase contains vitreous inclusions before $^{40}Ar/^{39}Ar$ dating is used.

6. Conclusion

1. We conducted $^{40}Ar/^{39}Ar$ analyses on the fallout tephra from core 1396A of the IODP 340 mission, and the samples that yielded abnormal young $^{40}Ar/^{39}Ar$ ages were examined.

2. Based on FESEM images, glass was widely present in the hornblendes and plagioclases but in different forms. The glass was predominantly found in the edges surrounding the hornblendes, whereas the glass existed inside plagioclase, mainly as vitreous inclusions.

3. Based on electron microprobe and energy spectrum analyses, the K content of glass was several orders of magnitude greater than that of hornblende and plagioclase and provided a considerable contribution to radiogenic ^{40}Ar.

4. Based on the K distribution in the different samples, we proposed that the abnormally high K content in the glass resulted from alternation with seawater and could cause inaccurate young $^{40}Ar/^{39}Ar$ ages for some hornblendes and plagioclases and there is no significant Ar loss that occurred in the hornblende and plagioclase during the post-eruption period.

5. Based on the age spectra and K/Ca ratios of samples, altered glass tends to have a greater impact on the age of hornblende and plagioclase during low-temperature stages.

6. We designed a pretreatment method for the submarine hornblende sample dating to reduce the effect from the glass. The second-round $^{40}Ar/^{39}Ar$ analyses confirmed the validity of this method. We also deduced that not all submarine plagioclase samples were suitable for $^{40}Ar/^{39}Ar$ dating.

Data availability

All the data underlying this article will be shared on reasonable request to the corresponding author.

Author contributions

Conceptualization: Zhiyu Han; Fei Wang, data curation: Zhiyu Han, formal analysis: Zhiyu Han; Wenbei Shi; Yinzhi Wang, funding acquisition: Fei Wang, investigation: Zhiyu Han, methodology: Zhiyu Han; Fei Wang; Liekun Yang, project administration: Zhiyu Han; Fei Wang, resources: Liekun Yang; Fei Wang, software: Zhiyu Han; Wenbei Shi, supervision: Fei Wang; Liekun Yang, validation: Zhiyu Han, visualization: Zhiyu Han, writing – original draft: Zhiyu Han, and writing – review & editing: Zhiyu Han; Fei Wang; Wenbei Shi.

Conflicts of interest

Competing interest declaration: the authors have no competing interests to declare that are relevant to the content of this article.

Acknowledgements

This research was funded by the Natural Science Foundation of China (41930106). Thanks to all the scientists involved in the IODP 340 Expedition.

References

1 W. C. Pitman and M. Talwani, Sea-floor spreading in the North Atlantic, *GSA Bull.*, 1972, **83**(3), 619–646, DOI: 10.1130/0016-7606(1972)83[619:SSITNA]2.0.CO;2.

2 R. D. Jarrard, Relations among subduction parameters, *Rev. Geophys.*, 1986, **24**(2), 217–284, DOI: 10.1029/RG024i002p00217.

3 C. W. Devey, F. Albarede, J. L. Cheminée, *et al.*, Active submarine volcanism on the society hotspot swell (west Pacific): a geochemical study, *J. Geophys. Res. Solid Earth*, 1990, **95**(B4), 5049–5066, DOI: 10.1029/JB095iB04p05049.

4 K. Saito and M. Ozima, ^{40}Ar–^{39}Ar geochronological studies on submarine rocks from the western Pacific area, *Earth Planet. Sci. Lett.*, 1977, **33**(3), 353–369, DOI: 10.1016/0012-821X(77)90087-5.

5 C.-F. Li, X. Xu, J. Lin, *et al.*, Ages and magnetic structures of the South China sea constrained by deep tow magnetic surveys and IODP expedition 349, *Geochem. Geophys. Geosyst.*, 2014, **15**(12), 4958–4983, DOI: 10.1002/2014GC005567.

6 R. Hickey-Vargas, G. M. Yogodzinski, O. Ishizuka, *et al.*, Origin of depleted basalts during subduction initiation and early development of the Izu-Bonin-Mariana island arc: evidence from IODP expedition 351 site U1438, amami-sankaku basin, *Geochim. Cosmochim. Acta*, 2018, **229**, 85–111, DOI: 10.1016/j.gca.2018.03.007.

7 M. K. Reagan, D. E. Heaton, M. D. Schmitz, *et al.*, Forearc ages reveal extensive short-lived and rapid seafloor spreading following subduction initiation, *Earth Planet. Sci. Lett.*, 2019, 506520–506529, DOI: 10.1016/j.epsl.2018.11.020.

8 I. McDougall and T. M. Harrison, *Geochronology and Thermochronology by the $^{40}Ar/^{39}Ar$ Method*, Oxford University Press, USA, 1999.

9 J. Dymond and L. Windom H, Cretaceous K–Ar ages from Pacific Ocean seamounts, *Earth Planet. Sci. Lett.*, 1968, **4**(1), 47–52, DOI: 10.1016/0012-821X(68)90052-6.

10 M. Ozima, I. Kaneoka and S. Aramaki, K–Ar ages of submarine basalts dredged from seamounts in the western pacific area and discussion of oceanic crust, *Earth Planet. Sci. Lett.*, 1970, **8**(3), 237–249, DOI: 10.1016/0012-821X(70)90183-4.

11 I. Kaneoka, The effect of hydration on the K/Ar ages of volcanic rocks, *Earth Planet. Sci. Lett.*, 1972, **14**(2), 216–220, DOI: 10.1016/0012-821X(72)90009-X.

12 M. Ozima, K. Saito, M. Honda, *et al.*, Sea water weathering effect on K–Ar age of submarine basalts, *Geochim. Cosmochim. Acta*, 1977, **41**(4), 453–461, DOI: 10.1016/0016-7037(77)90284-8.

13 D. E. Seidemann, Effects of submarine alteration on K–Ar dating of deep-sea igneous rocks, *GSA Bull.*, 1977, **88**(11),

1660–1666, DOI: 10.1130/0016-7606(1977)88<1660:EOSAOK>2.0.CO;2.
14 W. G. Melson and G. Thompson, Glassy abyssal basalts, atlantic sea floor near St. Paul's rocks: petrography and composition of secondary clay minerals, *GSA Bull.*, 1973, **84**(2), 703–716, DOI: 10.1130/0016-7606(1973)84<703:GABASF>2.0.CO;2.
15 D. A. Clague, J. B. Paduan, W. C. McIntosh, *et al.*, A submarine perspective of the Honolulu Volcanics, Oahu, *J. Volcanol. Geotherm. Res.*, 2006, **151**(1), 279–307, DOI: 10.1016/j.jvolgeores.2005.07.036.
16 B. R. Jicha, J. M. Rhodes, B. S. Singer, *et al.*, $^{40}Ar/^{39}Ar$ geochronology of submarine Mauna Loa volcano, Hawaii, *J. Geophys. Res. Solid Earth*, 2012, **117**(B9), DOI: 10.1029/2012JB009373.
17 K. Sato, H. Kawabata, W. Scholl D, *et al.*, ^{40}Ar–^{39}Ar dating and tectonic implications of volcanic rocks recovered at IODP Hole U1342A and D on Bowers Ridge, Bering Sea, *Deep Sea Res., Part II*, 2016, **125**, 126214–126226, DOI: 10.1016/j.dsr2.2015.03.008.
18 R. Bezard, K. Hoernle, J. A. Pfänder, *et al.*, $^{40}Ar/^{39}Ar$ ages and bulk-rock chemistry of the lower submarine units of the central and western Aleutian Arc, *Lithos*, 2021, **392–393**, 106147, DOI: 10.1016/j.lithos.2021.106147.
19 K. C. Macdonald and T. L. Holcombe, Inversion of magnetic anomalies and sea-floor spreading in the Cayman Trough, *Earth Planet. Sci. Lett.*, 1978, **40**(3), 407–414, DOI: 10.1016/0012-821X(78)90163-2.
20 N. Feuillet, I. Manighetti, P. Tapponnier, *et al.*, Arc parallel extension and localization of volcanic complexes in Guadeloupe, Lesser Antilles, *J. Geophys. Res. Solid Earth*, 2002, **107**(B12), ETG3, DOI: 10.1029/2001JB000308.
21 J. C. Briden, D. C. Rex, A. M. Faller, *et al.*, K-Ar geochronology and palaeomagnetism of volcanic rocks in the Lesser Antilles island arc, *Philos. Trans. R. Soc., A*, 1979, **291**, 485–528, DOI: 10.1098/rsta.1979.0040.
22 P. Bouysse and D. Westercamp, Subduction of atlantic aseismic ridges and late cenozoic evolution of the lesser antilles island arc, *Tectonophysics*, 1990, **175**(4), 349–380, DOI: 10.1016/0040-1951(90)90180-G.
23 R. Macdonald, C. J. Hawkesworth and E. Heath, The lesser antilles volcanic chain: a study in arc magmatism, *Earth-Sci. Rev.*, 2000, **49**(1), 1–76, DOI: 10.1016/S0012-8252(99)00069-0.
24 Expedition 340 Scientists, Lesser Antilles volcanism and landslides: implications for hazard assessment and long-term magmatic evolution of the arc, *IODP Prel. Rep.*, 2012, **340**, DOI: 10.2204/iodp.pr.340.2012.
25 A. Le Friant, O. Ishizuka, G. Boudon, *et al.*, Submarine record of volcanic island construction and collapse in the Lesser Antilles arc: first scientific drilling of submarine volcanic island landslides by IODP Expedition 340, *Geochem. Geophys. Geosyst.*, 2015, **16**(2), 420–442, DOI: 10.1002/2014GC005652.
26 M. R. Palmer, S. J. Hatter, T. M. Gernon, *et al.*, Discovery of a large 2.4 Ma Plinian eruption of Basse-Terre, Guadeloupe, from the marine sediment record, *Geology*, 2016, **44**(2), 123–126, DOI: 10.1130/G37193.1.
27 F. Zami, X. Quidelleur, J. Ricci, *et al.*, Initial sub-aerial volcanic activity along the central Lesser Antilles inner arc: new K–Ar ages from Les Saintes volcanoes, *J. Volcanol. Geotherm. Res.*, 2014, 28712–28721, DOI: 10.1016/j.jvolgeores.2014.09.011.
28 C. L. Harford, M. S. Pringle, R. S. J. Sparks, *et al.*, *The Volcanic Evolution of Montserrat Using 40Ar/39Ar Geochronology*, ed. T. H. Druitt, Geological Society of London, Kokelaar, 2002, DOI: 10.1144/GSL.MEM.2002.021.01.05.
29 A. Samper, X. Quidelleur, P. Lahitte, *et al.*, Timing of effusive volcanism and collapse events within an oceanic arc island: Basse-Terre, Guadeloupe archipelago (Lesser Antilles Arc), *Earth Planet. Sci. Lett.*, 2007, **258**(1), 175–191, DOI: 10.1016/j.epsl.2007.03.030.
30 R. G. Hatfield, Data report: stratigraphic correlation of Site U1396 and creation of a composite depth scale and splice, in *Proceedings of the Integrated Ocean Drilling Program*, ed. L. Friant, *et al.*, Integrated Ocean Drilling Program Management International, Inc., Tokyo, 2015, p. 340, DOI: 10.2204/iodp.proc.340.202.
31 M. Cassidy, S. F. L. Watt, M. R. Palmer, *et al.*, Construction of volcanic records from marine sediment cores: a review and case study (Montserrat, West Indies), *Earth Sci. Rev.*, 2014, **138**, 137–155, DOI: 10.1016/j.earscirev.2014.08.008.
32 F. Wang, F. Jourdan, C.-H. Lo, *et al.*, YBCs sanidine: a new standard for $^{40}Ar/^{39}Ar$ dating, *Chem. Geol.*, 2014, **388**, 87–97, DOI: 10.1016/j.chemgeo.2014.09.003.
33 R. H. Steiger and E. Jäger, Subcommission on geochronology: convention on the use of decay constants in geo- and cosmochronology, *Earth Planet. Sci. Lett.*, 1977, **36**(3), 359–362, DOI: 10.1016/0012-821X(77)90060-7.
34 A. A. P. Koppers, ArArCALC—software for $^{40}Ar/^{39}Ar$ age calculations, *Comput. Geosci.*, 2002, **28**(5), 605–619, DOI: 10.1016/S0098-3004(01)00095-4.
35 G. P. L. Walker, L. Wilson and E. L. G. Bowell, Explosive volcanic eruptions—I the rate of fall of pyroclasts, *Geophys. J. Int.*, 1971, **22**(4), 377–383, DOI: 10.1111/j.1365-246X.1971.tb03607.x.
36 L. Wilson and G. P. L. Walker, Explosive volcanic eruptions – VI. Ejecta dispersal in plinian eruptions: the control of eruption conditions and atmospheric properties, *Geophys. J. Int.*, 1987, **89**(2), 657–679, DOI: 10.1111/j.1365-246X.1987.tb05186.x.
37 V. Manville, K. Németh and K. Kano, Source to sink: a review of three decades of progress in the understanding of volcaniclastic processes, deposits, and hazards, *Sediment. Geol.*, 2009, **220**(3), 136–161, DOI: 10.1016/j.sedgeo.2009.04.022.
38 H. Sigurdsson, R. S. J. Sparks, S. N. Carey, *et al.*, Volcanogenic sedimentation in the lesser antilles arc, *J. Geol.*, 1980, **88**(5), 523–540, DOI: 10.1086/628542.
39 S. Carey and H. Sigurdsson, A model of volcanogenic sedimentation in marginal basins, *Geol. Soc. Spec. Publ.*, 1984, **16**, 37–58, DOI: 10.1144/GSL.SP.1984.016.01.04.

40 R. Pamela Reid, S. N. Carey and D. R. Ross, Late quaternary sedimentation in the Lesser Antilles island arc, *GSA Bull.*, 1996, **108**(1), 78–100, DOI: 10.1130/0016-7606(1996)108<0078:LQSITL>2.3.CO;2.

41 A. Le Friant, C. L. Harford, C. Deplus, *et al.*, Geomorphological evolution of Montserrat (West Indies): importance of flank collapse and erosional processes, *J. Geol. Soc.*, 2004, **161**(1), 147–160, DOI: 10.1144/0016-764903-017.

42 A. J. Schaen, B. R. Jicha, K. V. Hodges, *et al.*, Interpreting and reporting $^{40}Ar/^{39}Ar$ geochronologic data, *GSA Bull.*, 2020, **133**(3–4), 461–487, DOI: 10.1130/B35560.1.

43 J.-Y. Lee, K. Marti, J. P. Severinghaus, *et al.*, A redetermination of the isotopic abundances of atmospheric Ar, *Geochim. Cosmochim. Acta*, 2006, **70**(17), 4507–4512, DOI: 10.1016/j.gca.2006.06.1563.

44 I. Friedman and W. Long, Volcanic glasses, their origins and alteration processes, *J. Non-Cryst. Solids*, 1984, **67**(1), 127–133, DOI: 10.1016/0022-3093(84)90144-3.

45 H. Staudigel and S. R. Hart, Alteration of basaltic glass: mechanisms and significance for the oceanic crust-seawater budget, *Geochim. Cosmochim. Acta*, 1983, **47**(3), 337–350, DOI: 10.1016/0016-7037(83)90257-0.

46 T. H. Staudacher, E. K. Jessberger, B. Dominik, *et al.*, ^{40}Ar-^{39}Ar ages of rocks and glasses from the Noerdlinger Ries crater and the temperature history of impact breccias, *J. Geophys.*, 1982, **51**(1), 1–11.

47 A. Mulch, M. Cosca and M. Handy, *In situ* UV-laser $^{40}Ar/^{39}Ar$ geochronology of a micaceous mylonite : an example of defect-enhanced argon loss, *Contrib. Mineral. Petrol.*, 2002, **142**(6), 738–752, DOI: 10.1007/s00410-001-0325-6.

48 S. Kelley, K–Ar and Ar–Ar Dating, *Rev. Mineral. Geochem.*, 2002, **47**(1), 785–818, DOI: 10.2138/rmg.2002.47.17.

49 K. A. Foland, T. H. Fleming, A. Heimann, *et al.*, Potassium-argon dating of fine-grained basalts with massive Ar loss: application of the $^{40}Ar^{39}Ar$ technique to plagioclase and glass from the Kirkpatrick Basalt, Antarctica, *Chem. Geol.*, 1993, **107**(1), 173–190, DOI: 10.1016/0009-2541(93)90109-V.

50 A. A. P. Koppers, H. Staudigel and J. R. Wijbrans, Dating crystalline groundmass separates of altered Cretaceous seamount basalts by the $^{40}Ar/^{39}Ar$ incremental heating technique, *Chem. Geol.*, 2000, **166**(1), 139–158, DOI: 10.1016/S0009-2541(99)00188-6.

51 A. A. P. Koppers, J. A. Russell, J. Roberts, *et al.*, Age systematics of two young en echelon Samoan volcanic trails, *Geochem. Geophys. Geosyst.*, 2011, **12**(7), Q07025, DOI: 10.1029/2010GC003438.

52 H.-N. Qiu and Y.-D. Jiang, Sphalerite $^{40}Ar/^{39}Ar$ progressive crushing and stepwise heating techniques, *Earth Planet. Sci. Lett.*, 2007, **256**(1), 224–232, DOI: 10.1016/j.epsl.2007.01.028.

53 J.-W. Zi, P. W. Haines, X.-C. Wang, *et al.*, Pyroxene $^{40}Ar/^{39}Ar$ dating of basalt and applications to large igneous provinces and precambrian stratigraphic correlations, *J. Geophys. Res. Solid Earth*, 2019, **124**(8), 8313–8330, DOI: 10.1029/2019JB017713.

54 F. Jourdan and P. R. Renne, Neutron-induced ^{37}Ar recoil ejection in *Ca-rich Minerals and Implications for $^{40}Ar/^{39}Ar$ Dating*, ed. F. Jourdan, D. F. Mark and C. Verati, Geological Society of London, 2014, DOI: 10.1144/SP378.

55 T. C. Onstott, M. L. Miller, R. C. Ewing, G. W. Arnold and D. S. Walsh, Recoil refinements: implications for the $^{40}Ar/^{39}Ar$ dating technique, *Geochim. Cosmochim. Acta*, 1995, **59**(9), 1821–1834, DOI: 10.1016/0016-7037(95)00085-E.

56 I. M. Villa, Direct determination of ^{39}Ar recoil distance, *Geochim. Cosmochim. Acta*, 1997, **61**(3), 689–691, DOI: 10.1016/S0016-7037(97)00002-1.